

Journal of  
**Micro/Nanolithography,  
MEMS, and MOEMS**

[SPIEDigitalLibrary.org/jm3](http://SPIEDigitalLibrary.org/jm3)

## **Review of resist-based flare measurement methods for extreme ultraviolet lithography**

Lei Sun  
Obert R. Wood  
Erik A. Verduijn  
Mandeep Singh  
Wenhui Wang  
Ryoung-Han Kim  
Pawitter Mangat  
Hui Peng Koh  
Harry J. Levinson

# Review of resist-based flare measurement methods for extreme ultraviolet lithography

**Lei Sun**  
**Obert R. Wood**  
GLOBALFOUNDRIES  
257 Fuller Road, Suite 3100  
Albany, New York 12203  
E-mail: [Lei.Sun@globalfoundries.com](mailto:Lei.Sun@globalfoundries.com)

**Erik A. Verduijn**  
**Mandeep Singh**  
GLOBALFOUNDRIES  
Kapeldreef 75  
B-3001 Leuven, Belgium

**Wenhui Wang**  
**Ryoung-Han Kim**  
**Pawitter Mangat**  
**Hui Peng Koh**  
GLOBALFOUNDRIES  
257 Fuller Road, Suite 3100  
Albany, New York 12203

**Harry J. Levinson**  
GLOBALFOUNDRIES  
1050 Arques Avenue  
Sunnyvale, California 95085

**Abstract.** Flare (stray light) is an important effect impacting extreme ultraviolet lithography (EUVL) imaging system performance. Four flare measurement methods including Kirk, modulation transfer function, double exposure, and zonal ring approximation method are reviewed and analyzed theoretically. The point spread function of an EUV NXE:3100 exposure tool is extracted from the measured Kirk flare (KF) and fitted with a double-fractal model. The KF for this NXE:3100 tool is determined to be 8.5% for a 2- $\mu\text{m}$  diameter absorber pad placed in a 12-mm outer radius bright field, which is larger than the previous 5% KF data measured by ASML and IMEC in 2011. The observation of the increased flare level in the NXE:3100 tool suggests that contamination of EUV optics may be a potential problem for EUVL manufacturing. © The Authors. Published by SPIE under a Creative Commons Attribution 3.0 Unported License. Distribution or reproduction of this work in whole or in part requires full attribution of the original publication, including its DOI. [DOI: [10.1117/1.JMM.12.4.042001](https://doi.org/10.1117/1.JMM.12.4.042001)]

Subject terms: nanolithography; stray light; flare; out-of-band; extreme ultraviolet.

Paper 13170 received Sep. 19, 2013; revised manuscript received Oct. 29, 2013; accepted for publication Nov. 4, 2013; published online Dec. 17, 2013.

## 1 Introduction

Extreme ultraviolet lithography (EUVL) is a next generation lithography technology which is scheduled to be inserted into semiconductor device manufacturing beyond the 10-nm technology node.<sup>1–4</sup> Compared with the 248- and 193-nm wavelengths used in deep ultraviolet lithography (DUVL), a 13.5-nm wavelength is used in EUVL. Only reflective optical components and masks can be used in EUVL, because most materials strongly absorb 13.5-nm light. Before EUVL can be inserted into manufacturing, many problems need to be solved, such as flare, optical proximity correction, horizontal and vertical print difference (HVPD), defectivity, optical source power, overlay, etc.<sup>2</sup> Among these problems, flare is one of the important remaining issues that needs to be addressed.

Flare, which is also called the stray light, is due to light scattered by lens inhomogeneity and surface roughness. This kind of light can be scattered from bright areas to all the other areas of the image, including areas that are supposed to be dark. Flare provides a localized background light intensity which can induce critical dimension (CD) variation and reduce contrast and process window.<sup>5,6</sup>

Even though this effect has been studied and is well understood in KrF (248 nm) and ArF (193 nm) lithographies, not much attention has been paid to it recently because the level of flare has been sufficiently suppressed and the resultant impact to lithography processes is small. When the lithography wavelength shifts from 193 to 13.5 nm, flare can no longer be neglected. One reason is that scattered light is

inversely proportional to the square of the wavelength, which means that the flare level would increase 200-fold when migrating from 193 to 13.5 nm if surface roughness remains constant. Another reason is that light interacts twice with the surfaces of EUV optical components, whereas it interacts only once with DUV lenses due to the use of reflective optics in the EUV spectral region. For these reasons, the flare level has increased from 2% to 3% in DUVL<sup>7</sup> to 14% in EUVL.<sup>8</sup> Therefore, it is critically important to address the flare problem in EUVL.

The EUVL projection optics mirror vendors usually characterize flare directly by measuring the mirror surface with an interferometer, a microscope, and an atomic force microscope (AFM).<sup>9,10</sup> However, it is more practical for end users to measure flare using a resist-based method, which means measuring flare patterns exposed on a resist-coated wafer with a CD scanning electron microscope (CD SEM). Four resist-based flare measurement methods have been proposed including Kirk,<sup>11–13</sup> modulation transfer function (MTF),<sup>14–17</sup> double exposure,<sup>18,19</sup> and zonal ring approximation method (ZRAM),<sup>20</sup> and all four methods will be reviewed in this article. Knowledge of the flare point spread function (PSF) is important when modifying the mask patterns to compensate for flare.<sup>21,22</sup> However, the detailed relationships between measured flare and PSF have not yet been published for these methods. How to derive PSF from measurement will also be shown in this article.

The flare levels in the latest generation of EUV full-field scanners, the ASML NXE:3100, which is installed in IMEC

Belgium, are evaluated using the Kirk method. The flare PSF of the NXE:3100 is extracted from the measurement and fitted with a double-fractal model.

## 2 Flare Theory

Flare is caused by light scattering from contamination, multiple reflections, lens inhomogeneity, and surface roughness. The surface roughness contributes most and can be classified into three categories: low-spatial frequency roughness (LSFR) with spatial frequencies  $<10^{-6} \text{ nm}^{-1}$ , middle SFR (MSFR) with spatial frequencies between  $10^{-6} \text{ nm}^{-1}$  and  $10^{-3} \text{ nm}^{-1}$ , and high SFR (HSFR) with spatial frequencies  $>10^{-3} \text{ nm}^{-1}$ .<sup>2,10,22,23</sup> Light scattering can also be classified correspondingly into three categories due to the spatial frequency difference of surface roughness.<sup>11</sup> The short range scattering is generated from LSFR and has a submicrometer influence range. The LSFR is also a source for aberrations. The middle range scattering is generated from MSFR and has an influence range from sub micrometer to millimeter scales. It degrades printed CD accuracy and reduces contrast and process window more than any other effect. The flare, which people care most about, also refers to this middle-range scattering. Long-range scattering is generated by HSFR and has an influence range of larger than millimeter scale. Some of the long-range scattering is blocked by the exit pupil of the imaging system and can be regarded as a reflection loss, and some goes through the exit pupil and can be regarded as background scattering intensity.

An optical system can usually be characterized by its PSF, which is the response of the optical system to a point source. In the absence of scattering, the PSF is diffraction limited and is usually expressed as an Airy function. The PSF with scattering is shown in Fig. 1. The image light intensity profile of a point source after an optical system can be divided into three parts. The diffraction- and aberration-induced PSF region is from 0 to  $r_{\min}$ . The region from  $r_{\min}$  to  $r_{\max}$  is the flare region. The energy-loss region is beyond  $r_{\max}$ . Only the positive axis region is shown in Fig. 1 since rotational symmetry has been assumed. The  $r_{\min}$  and  $r_{\max}$  are submicrometer and millimeter scales, respectively, as

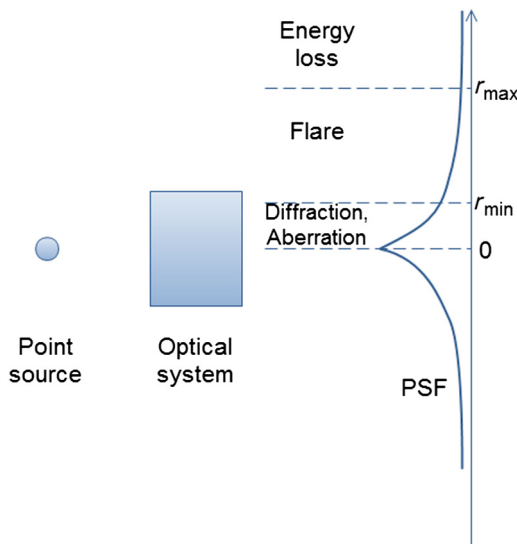


**Fig. 1** Different point spread function (PSF) regions in a scattering optical system.

mentioned in the above paragraph. The PSF used in the rest of this article will refer to the flare-related PSF only.

The PSF expresses the system performance in the spatial domain. Another well-known function, MTF, expresses system performance in the frequency domain. The PSF and MTF are a Fourier pair.  $\text{MTF} = \mathfrak{F}\{\text{PSF}\}$  and  $\text{PSF} = \mathfrak{F}^{-1}\{\text{MTF}\}$ , where  $\mathfrak{F}\{\}$  and  $\mathfrak{F}^{-1}\{\}$  are Fourier and inverse Fourier transforms, respectively. Thus, PSF can be calculated from the measured MTF, and this measurement method will be discussed later. Another commonly used parameter by mirror vendors is power spectral density (PSD), which describes how the power of a signal is distributed with frequency. The PSD is equal to the square of the amplitude of the MTF,  $\text{PSD} = |\text{MTF}|^2$ . The autocorrelation of PSF is also a Fourier pair with PSD. A more detailed relationship between PSF and PSD can be found in the literature.<sup>2,10,23</sup>

There are three empirical models for PSF: Gaussian, ABC, and fractal.<sup>7</sup> If double-scattering processes are present, these models expand to double Gaussian, double ABC, and double-fractal functions, as shown in Table 1. The single coordinate  $r$  is used because PSF is assumed to have rotational symmetry. Constants  $w_1$ ,  $w_2$ ,  $k_1$ ,  $k_2$ , and  $A$  are scale factors. Spectral indexes  $n_1$  and  $n_2$  usually range from 1 to 3.  $B$ ,  $r_t$ ,  $\sigma_1$ , and  $\sigma_2$  are also constants. When  $w_2$  or  $k_2 = 0$ , the double PSF model is simplified to a single PSF model. The ABC model is very similar to the fractal model, except in the small  $r$  region. Their expressions will be the same when  $B r^2 \gg 1$ . Therefore, the fractal model can be regarded as a simplified version of the ABC model and is used as the second PSF term in the ABC model in Table 1. The PSF usually has a long tail extending to the millimeter dimension. This tail in the Gaussian model decays quickly. Thus, the Gaussian model is usually not as accurate as the fractal model.<sup>5</sup> For these reasons, the fractal model, which is simple and accurate, is preferred in most cases.

The total image intensity with flare  $I_1(x, y)$  can be calculated from Eqs. (1) and (2)<sup>10,23</sup>

$$I_1(x, y) = (1 - \text{TIS})I_0(x, y) + I_{\text{flare}}(x, y) \quad (1)$$

$$\begin{aligned} I_{\text{flare}}(x, y) &= \text{PSF}^{\text{SC}}(x, y) \otimes I_0(x, y) \\ &= \int \int_{-\infty}^{\infty} \text{PSF}^{\text{SC}}(x', y') I_0(x - x', y - y') dx' dy', \end{aligned} \quad (2)$$

where  $I_0(x, y)$  and  $I_{\text{flare}}(x, y)$  are the ideal total image intensity without flare and the intensity of the flare-induced image

**Table 1** Three models of PSF function.

PSF models	Equations
Gaussian	$\frac{1}{\sqrt{2\pi}} \left\{ \frac{w_1}{\sigma_1} \exp\left(\frac{-r^2}{2\sigma_1^2}\right) + \frac{w_2}{\sigma_2} \exp\left(\frac{-r^2}{2\sigma_2^2}\right) \right\}$
ABC	$\begin{cases} \frac{A}{(1 + B r^2)^{(n_1+1)/2}} & r < r_t \\ \frac{K_2}{r^{n_2+1}} & r > r_t \end{cases}$
Fractal	$\begin{cases} 0 & r < r_{\min} \\ \frac{K_1}{r^{n_1+1}} + \frac{K_2}{r^{n_2+1}} & r_{\max} > r > r_{\min} \end{cases}$

blur, respectively.  $\text{PSF}^{\text{SC}}(x, y)$  is the point spread function reaching the wafer.  $\otimes$  means convolution. TIS is the total integrated scatter indicating total intensity loss by scattering, which can be calculated as

$$\text{TIS} = \iint_{-\infty}^{+\infty} \text{PSF}^{\text{SC}0}(x, y) dx dy = \int_0^{+\infty} 2\pi r \text{PSF}^{\text{SC}0}(r) dr, \quad (3)$$

where  $\text{PSF}^{\text{SC}0}(x, y)$  is the point spread function scattered from the mirror. The first and the second terms in Eq. (1) represent intensity loss due to scattering and image blur due to flare, respectively.

Before 2010,  $\text{PSF}^{\text{SC}}(x, y)$  was directly used in Eq. (3). In 2010, Murakami et al. proposed that the PSFs for light scattered from a mirror ( $\text{PSF}^{\text{SC}0}$ ) and reaching the wafer ( $\text{PSF}^{\text{SC}}$ ) are different.<sup>10,23</sup> The reason for this is that some scattered light from a mirror may be blocked by internal obscurations such as apertures, mounting hardware, mirror-coating area, and flare stops in a scanner. Only a portion of the scattered light from a mirror can reach the wafer, contributing to  $\text{PSF}^{\text{SC}}$ . Thus,  $\text{PSF}^{\text{SC}}$  should, in general, be less than  $\text{PSF}^{\text{SC}0}$ . The  $\text{PSF}^{\text{SC}0}$  was derived from the mirror PSD, and it can be separated from  $\text{PSF}^{\text{SC}}$  by an obscuration factor, as shown in Refs. 10 and 23. However, this method is not suitable for use by end users because resist-based methods can only measure  $\text{PSF}^{\text{SC}}$ , and it is difficult to find the difference between  $\text{PSF}^{\text{SC}}$  and  $\text{PSF}^{\text{SC}0}$  without resorting to other methods. For this reason,  $\text{PSF}^{\text{SC}}$  is assumed to be equal to  $\text{PSF}^{\text{SC}0}$  in most cases and PSF is used in the following sections.

### 3 Resist-Based Flare Measurement Methods

#### 3.1 Kirk Method

The Kirk method, which is also called the disappearing pad test, was first proposed by Kirk.<sup>11</sup> It is the most widely used flare test method now due to its simplicity. Island features

(pads) are used in this method, as shown in Fig. 2(a). One isolated absorber pad is placed in a large bright field, which in the case of EUVL is an area of multilayer (ML) reflection. The area covered by the absorber is a dark area and all other areas are bright. Figure 2(b) shows a large bright field surrounded by a dark field.  $I_D$  and  $I_B$  are the normalized light intensity in centers of dark and bright fields, respectively.  $r_D$  and  $r_B$  are the coordinates in the dark and bright fields, respectively. In an ideal case,  $I_D = 0$  and  $I_B = 1$  if we neglect diffraction. In the flare case, some light is scattered from the bright area to the dark area, resulting in  $I_D > 0$  and  $I_B < 1$ . The increase in  $I_D$  is due to flare, and the decrease in  $I_B$  is due to the energy loss from scattering. The only way for the light to reach the center absorber pad area in Fig. 2(a) is via flare. Thus, flare information can be extracted from the knowledge of  $I_D$  and  $I_B$ .

Suppose  $E_{\text{resist}}$  is the dose received by the resist that can clear the resist completely.  $E_B$  and  $E_D$  are the doses incident on the whole reticle which can clear the resist in the bright and dark fields, respectively. The parameters  $t_B$  and  $t_D$  are the exposure times to clear the resist in the bright and dark fields, respectively.  $I_{\text{reticle}}$  is the light intensity incident on the whole reticle and is a constant.  $E_{\text{resist}}$  in the bright and dark fields satisfies the relations:  $E_{\text{resist}} = E_B(E_{\text{resist}}/E_B) = E_B[(E_{\text{resist}}/t_B)/(E_B/t_B)] = E_B(I_B/I_{\text{reticle}})$  and  $E_{\text{resist}} = E_D(E_{\text{resist}}/E_D) = E_D[(E_{\text{resist}}/t_D)/(E_D/t_D)] = E_D(I_D/I_{\text{reticle}})$ . From these relations, we have  $I_D/I_B = E_B/E_D$ , which is the definition of the Kirk flare (KF), the dose need to clear the resist in a large bright area divided by the dose need to clear the resist under an absorber pad. Combining Eqs. (1), (2), and the definition of KF, KF can be written as

$$\text{KF} = \frac{E_B}{E_D} = \frac{I_D}{I_B} = \frac{I_1(r_D=0)}{I_1(r_B=0)} = \frac{(1 - \text{TIS})I_0(r_D=0) + \text{PSF}(r_D) \otimes I_0(r_D)|_{r_D=0}}{(1 - \text{TIS})I_0(r_B=0) + \text{PSF}(r_B) \otimes I_0(r_B)|_{r_B=0}}, \quad (4)$$

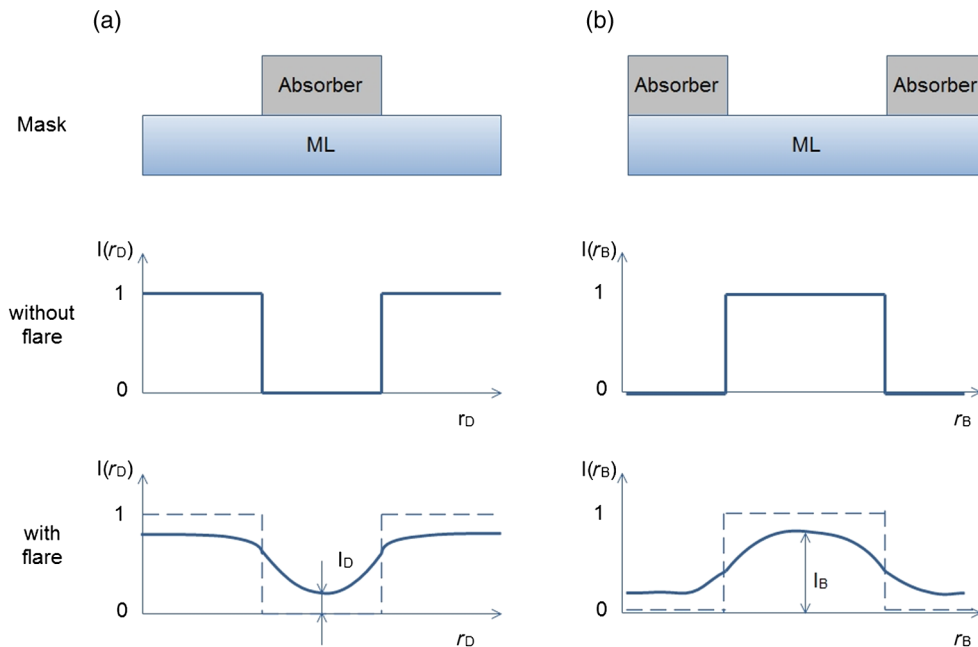


**Fig. 2** Plots of (a) a dark field surrounded by bright field and (b) a bright field surrounded by a dark field, respectively, on the mask and the corresponding aerial image light intensities with and without flare.

where  $I_D$  and  $I_B$  are calculated at different coordinates  $r_D$  and  $r_B$ .  $r_D = 0$  and  $r_B = 0$  correspond to the centers of the dark and bright areas, respectively.

A thin EUV mask absorber film is commonly used in order to minimize the HVPD. The residual EUV reflection from the absorber can be as much as 1% to 2% of the total EUV reflection light.<sup>24</sup> The EUV light source generally contains not only EUV, but also DUV light. Even with the insertion of spectral purity filters, a few percent of DUV light still remains. It can be reflected by the EUV mask and interacts with the resist. This problem is called Out-of-Band (OoB) radiation.<sup>25</sup> Since absorber EUV and OoB direct reflections are of the same magnitude as flare, they will be considered in the derivation. But the scattering of these two terms will be neglected, because they are too small to be compared with flare. Define  $I_0(r_D = 0) = I_{\text{abs}} + I_{\text{OoB}}$ , where  $I_{\text{abs}}$  and  $I_{\text{OoB}}$  are the light intensity from absorber EUV and OoB reflections, respectively.  $I_{\text{abs}}$  and  $I_{\text{OoB}}$  are neglected in  $I_B$ , because they are only a few percent of  $I_B$ .

The island features used for the Kirk method include squares, bars, and circular pads. The circular pad is most popular because of the rotational symmetry of the PSF and because of the calculational simplicity. The circular absorber pad is usually placed in a circular bright field which consists of a donut pattern. Figure 3 shows the donut pattern and the large bright field surrounded by a dark field used in the Kirk method, where  $r_0$  and  $r_1$  are the inner and outer radii of the donut, respectively.  $r_2$  is the radius of the large bright field.

Linear  $I_0$  terms appear in both the nominator and denominator in Eq. (4); thus normalized  $I_0$  can be used in this case. For simplicity, we assume  $I_0 = 1$  in a bright field and  $I_0 = 0$  in a dark field in the ideal case, since scattering of absorber EUV and OoB reflections have been neglected. Flare-induced image blur intensity in the nominator of Eq. (4) can be written as

$$\begin{aligned} \text{PSF}(r_D) \otimes I_0(r_D)|_{r_D=0} &= \int_0^\infty \text{PSF}(r)I_0(0-r)2\pi r dr \\ &\approx \int_0^{r_1} \text{PSF}(r)2\pi r dr, \end{aligned} \quad (5)$$

where  $I_0(r) = I_0(-r)$ , since the Kirk pad has rotational symmetry. Similarly, the flare-induced image blur intensity in the denominator of Eq. (4) can be approximated as

$$\text{PSF}(r_B) \otimes I_0(r_B)|_{r_B=0} \approx \int_0^{r_2} \text{PSF}(r)2\pi r dr. \quad (6)$$

If  $r_2$  is sufficiently large ( $r_2 \rightarrow \infty$ ), the convolution and the TIS in the denominator of Eq. (4) will cancel. In practice,

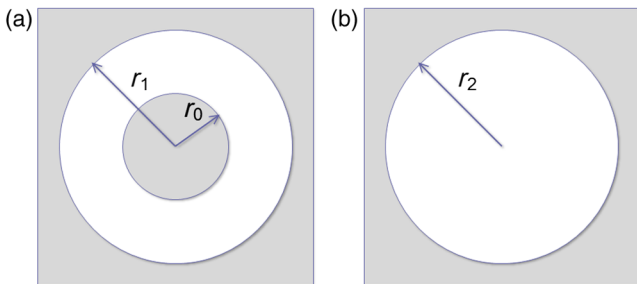


Fig. 3 (a) Donut pattern and (b) large bright field used in Kirk method.

the selection of  $r_2$  is also dependent on the PSF. Usually it needs to be larger than several millimeters to satisfy this approximation. With the  $r_2 \rightarrow \infty$  approximation, KF can be written as

$$\text{KF} = (1 - \text{TIS}) \frac{I_{\text{abs}} + I_{\text{OoB}}}{I_{\text{ML}}} + \int_{r_0}^{r_1} \text{PSF}(r)2\pi r dr, \quad (7)$$

where  $I_{\text{ML}} = I_0(r_B = 0)$  is the light intensity reflected from a large bright field of ML in EUVL. Equation (7) can be further simplified to

$$\text{KF} = (1 - \text{TIS}) \cdot \left( \frac{R_{\text{abs}}}{R_{\text{ML}}} + \frac{I_{\text{OoB}}}{I_{\text{ML}}} \right) + \int_{r_0}^{r_1} \text{PSF}(r)2\pi r dr, \quad (8)$$

where  $R_{\text{abs}}$  and  $R_{\text{ML}}$  are the EUV reflectivity of the absorber pad and the ML, respectively. The absorber EUV reflection term  $R_{\text{abs}}/R_{\text{ML}}$  and the OoB term  $I_{\text{OoB}}/I_{\text{ML}}$  are usually determined theoretically and experimentally, respectively.

If the flare level is very small, for example, when the flare level is around 2% to 3% as is the case in DUVL, TIS can be regarded as much smaller than 1 and the  $(1 - \text{TIS})$  term can be neglected in Eq. (8). The approximated KF is shown in Eq. (9).

$$\text{KF} = \frac{R_{\text{abs}}}{R_{\text{ML}}} + \frac{I_{\text{OoB}}}{I_{\text{ML}}} + \int_{r_0}^{r_1} \text{PSF}(r)2\pi r dr. \quad (9)$$

Since the fractal model is the most popular PSF model, a double-fractal PSF model is used in the rest of derivation, as shown in Eq. (10). It can be simplified into a single-fractal model by making  $K_2 = 0$ .

$$\text{PSF}(r) = \begin{cases} 0 & r < r_{\min} \\ \frac{K_1}{r^{n_1+1}} + \frac{K_2}{r^{n_2+1}} & r_{\max} > r > r_{\min} \end{cases}. \quad (10)$$

Combining Eqs. (8) and (10), KF can be written as

$$\begin{aligned} \text{KF} = \frac{E_B}{E_D} &= (1 - \text{TIS}) \cdot \left( \frac{R_{\text{abs}}}{R_{\text{ML}}} + \frac{I_{\text{OoB}}}{I_{\text{ML}}} \right) \\ &+ \frac{2\pi K_1}{(1 - n_1)} \left( r_1^{1-n_1} - r_0^{1-n_1} \right) + \frac{2\pi K_2}{(1 - n_2)} \left( r_1^{1-n_2} - r_0^{1-n_2} \right) \end{aligned} \quad (11)$$

$$\begin{aligned} \text{TIS} &= \int_0^{+\infty} \text{PSF}(r)2\pi r dr = \frac{2\pi K_1}{(1 - n_1)} \left( r_{\max}^{1-n_1} - r_{\min}^{1-n_1} \right) \\ &+ \frac{2\pi K_2}{(1 - n_2)} \left( r_{\max}^{1-n_2} - r_{\min}^{1-n_2} \right). \end{aligned} \quad (12)$$

Equations (11) and (12) are used to calculate PSF from KF. If a thick mask absorber is used, the absorber reflection term,  $R_{\text{abs}}/R_{\text{ML}}$ , can be neglected in Eq. (11). It can also be estimated from simulation or measured directly when a thin absorber is used. When KF is measured on a large dark field, which is the case with no flare ( $K_1 = K_2 = 0$ ), the first term in Eq. (11) can be measured directly. After considering the absorber reflection term, the OoB term,  $I_{\text{OoB}}/I_{\text{ML}}$ , can be estimated. After the first term in Eq. (11) is determined, PSF and TIS can also be calculated.

The OoB is usually measured with metal blades<sup>26</sup> or with a metal-coated mask.<sup>27</sup> From Table 1 in Ref. 27, 96% of the OoB is reflected from aluminum while almost no EUV light is reflected. At the same time, 60% and 39% of OoB can be reflected from the ML and the absorber, respectively. Although an aluminum-coated mask is a good option to measure OoB, a normal EUV mask with a large absorber area can also be used to estimate OoB taking into account the ratio result from Lorusso et al.<sup>27</sup> The OoB measured from aluminum indicates the total OoB in the EUVL system, while the OoB reflected from absorber and ML are closer to the real case, since the EUV mask absorption of OoB is included. The OoB from the absorber and the ML provides the lower and upper limits in cases where bright and dark fields are co-located on the mask.

One of the advantages of the Kirk method is its insensitivity to the type of resist used, because only the dose ratio is measured. Other advantages include simple pattern design and simple experimental technique. These advantages make the Kirk method the most popular flare measurement technique. There are two disadvantages of the Kirk method. One is that a large energy dose is required to measure a small KF. For example, if the  $E_B$  is 10 mJ/cm<sup>2</sup>,  $E_D$  will be 1000 mJ/cm<sup>2</sup> for 1% KF, which places a heavy burden on an EUV exposure tool. The solution to this problem is to use a fast resist. A fast resist is usually too sensitive to print normal features, but it can be used with the Kirk method. The reported smallest  $E_B$  is around 2 mJ/cm<sup>2</sup> (Ref. 26). If KF is about 1%,  $E_D$  is only 200 mJ/cm<sup>2</sup>, which is acceptable.

Resist metrology is also a problem for the Kirk method. The value for the dose-to-clear in a photoresist is traditionally determined by visually inspecting a series of CD SEM resist images exposed at different doses. Unfortunately, the value for the dose-to-clear determined by the visual inspection method is inevitably affected by person-to-person differences and a new method, independent of operator influence, is needed. Lorusso et al.<sup>26</sup> in 2009 proposed an automated algorithm to calculate  $E_B$  and  $E_D$ . The contrast of the pad images was plotted as a function of dose. The dose-to-clear was defined as the dose when contrast = 0 for the second time, as shown in Fig. 2 in Ref. 26. The contrast method was one of the nonvisual inspection methods for determining dose-to-clear and has been shown to work well in some cases.<sup>26</sup> However, because image contrast is affected by differences in the photoresist, under-layer coating material, postexposure baking conditions, and SEM settings, other experimental conditions may not yield the same results. LaFontaine et al. determined the dose-to-clear by the appearance of peaks of grating structures with scatterometry. However, this method can only be used with grating structures.<sup>17</sup>

In 2013, Sun et al. proposed a Fourier spectrum method to determine the dose-to-clear in a photoresist.<sup>28</sup> During dissolution, the exposed resist will reshape randomly or fragment into many small random shapes. The spatial frequency spectra of these random shapes are much different from those of the background noise images, which are SEM images of the resist when the resist has been completely dissolved. Since the Fourier spectrum method focuses on these random shapes instead of image contrast, it is not affected by the differences of resist, under-layer coating material, postexposure baking condition, and SEM settings, and results in a more general measurement method.

Discrete dose step will also induce metrology error. Suppose  $E_j$  is used in an energy meander exposure, where  $j = 1$  to  $n$ , and  $E_n$  is the final dose in the energy meander. The dose-to-clear lies between  $E_j$  and  $E_{j+1}$ . Then,  $E_{\text{dose-to-clear}} = (E_{j+1} + E_j)/2$ , and the uncertainty is  $\pm E_{\text{error}}$ , where  $E_{\text{error}} = (E_{j+1} - E_j)/2$ . The relative error of the dose-to-clear is  $[E_{\text{error}}/(E_{\text{dose-to-clear}})] = (E_{j+1} - E_j)/(E_{j+1} + E_j)$ . The smaller the energy meander step, the smaller the error.

### 3.2 MTF Method

Modulation transfer function (MTF) or contrast transfer function (CTF) methods were used to evaluate the performance of the projection optics in DUVL.<sup>14</sup> In 2002, LaFontaine and other researchers measured flare with this method.<sup>15,16,29</sup> The MTF is measured directly at various spatial frequencies instead of the PSF measured in other methods. Since MTF and PSF create a Fourier pair, one can be converted into the other by a Fourier transform.

The modulation or contrast of an image is defined by

$$\text{Modulation} = (I_{\max} - I_{\min})/(I_{\max} + I_{\min}), \quad (13)$$

where  $I_{\max}$  and  $I_{\min}$  are the maximum and minimum light intensity of the image, respectively. The MTF is defined by the ratio of image modulation and the object modulation, so  $\text{MTF} = \text{image modulation}/\text{object modulation}$ . For an EUV reticle, which corresponds to the object,  $I_{\max} = I \cdot R_{\text{ML}}$  and  $I_{\min} = I \cdot R_{\text{abs}}$ , where  $I$  is the incident EUV light on the reticle.  $R_{\text{abs}}$  is usually approximated as zero for a thick absorber. Thus, object modulation is approximated as one. The MTF is directly represented by the image modulation.

As discussed in Sec. 3.1, the light intensity ratio is equal to a dose ratio,  $I_{\min}/I_{\max} = E_B/E_D$ , where  $E_B$  and  $E_D$  mean the smallest dose-to-clear a bright field resist and the dose-to-clear a dark field resist, respectively. Combining Eq. (13) and this relation, the MTF is written as

$$\text{MTF}(f) = \frac{E_D(f) - E_B(f)}{E_D(f) + E_B(f)}, \quad (14)$$

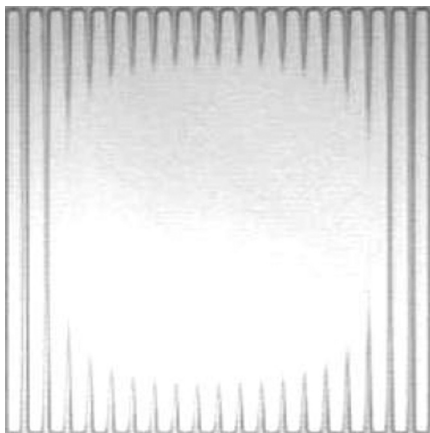
where  $f$  is the frequency at which MTF,  $E_B$ , and  $E_D$  are measured. A series of one-dimensional gratings have been used to measure MTF.<sup>15,16,29</sup> For a grating with uniform pitch, it has most of its modulation energy at the corresponding frequency as long as the grating area is sufficiently large. Therefore, even though finite-size gratings do not have a single-frequency spectrum, it is still a good approximation to regard the MTF measured at one grating as the MTF at the corresponding frequency. The MTF measured at a series of gratings with different pitches can be regarded as the MTF at different frequencies.  $E_B$  and  $E_D$  correspond to the dose-to-clear the resist in the trench and in the line of the grating, respectively. Experimentally,  $E_B$  can be defined as the dose corresponding to the largest grating contrast or the clearest grating.  $E_D$  can be defined as the dose to completely clear the grating. The area size of one uniform grating should be as large as possible for the single-frequency spectrum approximation to be valid. However, to make optimum use of the limited space on a reticle, this area size should be as small as possible. An optimized grating area size is required.

Figure 4 is an optical micrograph from LaFontaine et al.,<sup>15</sup> which shows that a 10- $\mu\text{m}$  pitch grating was removed in the center.

The MTF method was successfully used to measure flare in DUVL.<sup>15</sup> However, it may not be suitable for EUVL for three reasons. The first reason is cross-linking, which is a problem caused by one polymer chain linking to another with bonds in photoresist. It can arise in bright fields at large doses and should be avoided in measurement. Since the bright and dark fields are alternatively placed in a grating, the cross-linking can affect measurement results at large doses. The second reason is that a large dose is required for low-frequency gratings. One line in a grating can be regarded as the absorber pad or bar in the Kirk method. This line is placed in a bright field which is filled with 50% dark field, assuming a 1:1 grating. Therefore, the dose needed to clear this line, which is also the dose-to-clear the grating, is doubled in the MTF method compared with the dose in the Kirk method. The optical source power is not a problem in DUVL; however, it remains a bottleneck in EUVL at the present time. The third reason is that absorber EUV and OoB reflections are not considered in the MTF method. Flare result will not be accurate if these two factors are comparable to flare.

Three gratings with different frequencies were exposed in the EUV Alpha Demo Tool (ADT) in Albany, New York, to test the validity of the MTF method. A fast resist, Rohm and Haas XP4502J, was coated at 150-nm thickness on the wafer. All the gratings had 1:1 duty cycle, which means that the trench CD is equal to the line CD. Grating pitches were 80 nm, 600 nm, and 35  $\mu\text{m}$ , respectively, which correspond to high, middle, and low frequencies, respectively. Grating areas were  $50 \times 50 \mu\text{m}^2$  for 80 and 600-nm pitch gratings, respectively, and  $700 \times 700 \mu\text{m}^2$  for the 35- $\mu\text{m}$  pitch grating. The dose was increased from 5 to 164  $\text{mJ}/\text{cm}^2$  in the experiment.

Figure 5 shows the CD SEM images of these gratings at various doses. The 80-nm pitch grating is shown in Fig. 5(a). It is clear that the grating image is removed completely at 8  $\text{mJ}/\text{cm}^2$  dose. Resist cross-linking occurs above 36  $\text{mJ}/\text{cm}^2$ , but it does not affect the measurement result for this high-frequency grating. Figure 5(b) shows the CD SEM images of the 600-nm pitch grating. It looks as if the grating has been removed above 43  $\text{mJ}/\text{cm}^2$ .



**Fig. 4** Optical micrograph of a 10- $\mu\text{m}$  pitch grating used to measure modulation transfer function (MTF) in Ref. 15.

However, it is not easy to tell exactly when the grating is completely removed, because cross-linking is present at this dose level. Figure 5(c) shows the CD SEM images of the low-frequency grating. The grating does not change too much even with doses as high as 164  $\text{mJ}/\text{cm}^2$ . Cross-linking is not visible due to the low magnitude, although it is even worse at higher doses. A higher dose was not tested due to ADT productivity limits.

The above test shows that it is easy to measure MTF at high frequency but not at middle and low frequencies in EUVL. Since low-frequency term determines the limits of the PSF curve in the spatial domain, it is easy to have orders of magnitude error with wrong low-frequency measurement results. For example, PSF converted from MTF was one order of magnitude smaller than that measured from mirror roughness in Ref. 29.

The MTF method is very similar to the Kirk method. It is also resist independent and relies on visual inspection to determine the dose. The difference is that the Kirk method is measured in the spatial domain, whereas the MTF method is measured in the frequency domain. One advantage of the MTF method is that it is not measured with an empirical PSF model but directly converted from the MTF data.

### 3.3 Double-Exposure Method

The double-exposure method was proposed in 2001.<sup>18,19</sup> A reticle which contains a long thin line, e.g., 160-nm width, was initially exposed at a nominal dose. The line with 160-nm width should be imaged on the wafer after the first exposure, which is also called the imaging exposure. Then, another reticle is used for the second exposure on the same wafer, as shown in Fig. 6. This step is called the flare exposure. The only difference between the two reticles is that a thick line is used instead of the thin line at the same location. The width of the thick line is 1 to 16 times that of the thin line. The exposed thin line on the wafer should be covered by the thick line on the second reticle. If there is no flare, no light will be illuminated on the thin line on the wafer because of the thick line's shadow on the second reticle. Then, the thin line width should not change. If there is flare, flare-induced light will illuminate the thin line on the wafer and induce a line width change from which the flare can be calculated.

Thin-line CD change is measured as a function of dose in the flare exposure. Then, several local flare levels are input into lithography simulation software, e.g., PROLITH, and the thin-line CD change is simulated as a function of the flare exposure dose. The local flare level at which the experimental data and the simulation curve fit best can be determined as the final flare result. Figure 7 shows the experimental and curve fitting of the thin-line CD as a function of dose for a preproduction 193-nm scanner.<sup>19</sup> A 6% local flare value was determined for that scanner.

One of the advantages of the double-exposure method is that CD is directly measured instead of estimating via visual inspection of dose-to-clear as in the Kirk and MTF methods. Another advantage is that a small dose is used instead of a large dose, which is important when attempting to measure flare in a low-power EUV system. However, several reticles are used in the original design, which can increase the cost of the measurement. As an improved design, all the patterns can be on a single reticle. The reticle is shifted during the second

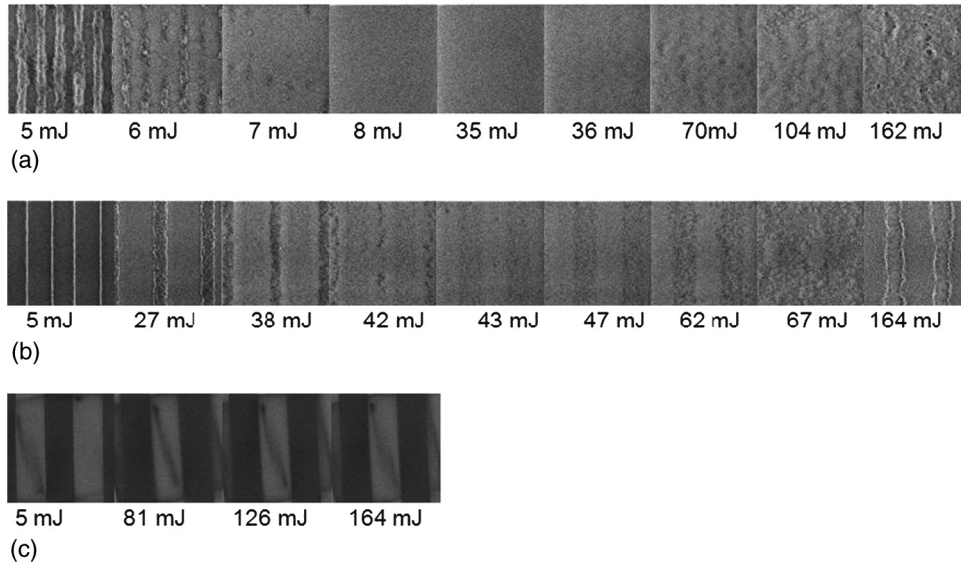


**Fig. 5** Critical dimension scanning electron microscope (CD SEM) images of different frequency gratings at various doses. (a) High frequency grating, (b) middle frequency grating, and (c) low frequency grating.

exposure instead of employing a second reticle. Overlay, CD uniformity (CDU), and line edge roughness (LER) can affect the measurement result. This method is heavily dependent on the accuracy of the optical and resist models used in the simulation software. Only local flare level was measured using an old version of PROLITH in 2002, and the PSF may be simulated using more recent versions of the simulation software.

### 3.4 ZRAM Method

The ZRAM was proposed in 2008.<sup>20</sup> Its principle is similar to that of the double-exposure method. Figure 8 shows ZRAM design.<sup>20</sup> It consists of a series of zonal rings and flare-sensing features in the center of the rings. Line and space patterns were used as the sensing features (gauging pattern) in Ref. 20. The circular area surrounding the gauging pattern is a bright field. The area outside the circular area is a dark field. The flare induced inside the circular area changes the line-width CD of the gauging pattern. Different circular radii correspond to different flare levels and different gauging pattern line widths.

The reference gauging pattern is a gauging pattern placed in a dark field, and the other gauging patterns are in the zonal rings. A line/space grating is used as the gauging pattern in Ref. 20. The first experimental step is to expose the reference

gauging pattern at various doses. Measurement of gauging pattern CD versus dose is used to create a look-up table. The second step is to expose all the zonal ring gauging patterns at a normal dose. The gauging pattern CD difference between reference gauging pattern and zonal ring gauging pattern is induced by the flare generated inside the zonal ring. The third is to convert the CD difference to dose using the Look-Up Table. The final step is to calculate the flare PSF based on the dose difference.

Assume  $I_{reticle}$  is the light intensity incident on the reticle.  $E_{norm}$  and  $\Delta E$  are the doses incident on the reticle at  $t_{norm}$  and  $\Delta t$  time, respectively. They have the relations

$$E_{norm} = I_{reticle}t_{norm} \tag{15}$$

$$E_{norm} + \Delta E = I_{reticle}(t_{norm} + \Delta t). \tag{16}$$

If the CD on the reference gauging pattern and the zonal ring gauging pattern is the same, then the same amount of dose,  $E'$ , is incident on the resist on these two patterns. Suppose the zonal ring gauging pattern is exposed with  $t_{norm}$  time, the reference gauging pattern needs to be exposed with extra time  $t_{norm} + \Delta t$  to have the same pattern CD.

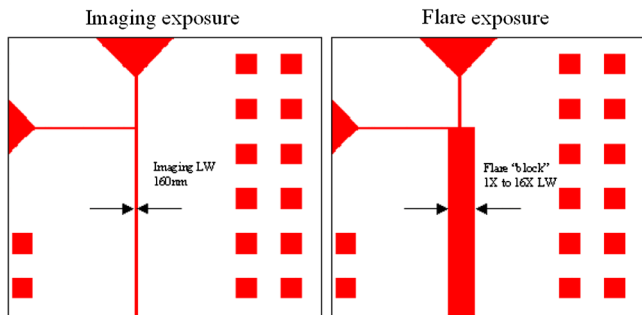


**Fig. 6** Two reticles used for double-exposure method.<sup>19</sup>

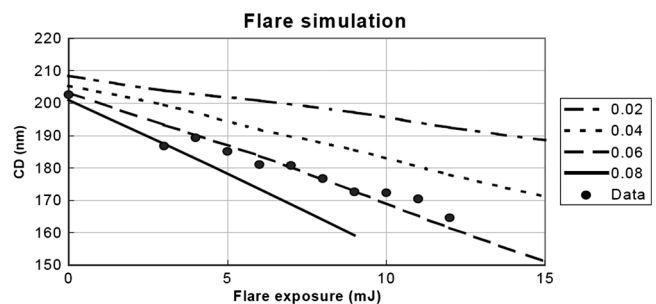


**Fig. 7** The experimental and curve fitting of the thin-line CD plotted as a function of dose in flare exposure for a preproduction 193-nm scanner.<sup>19</sup>

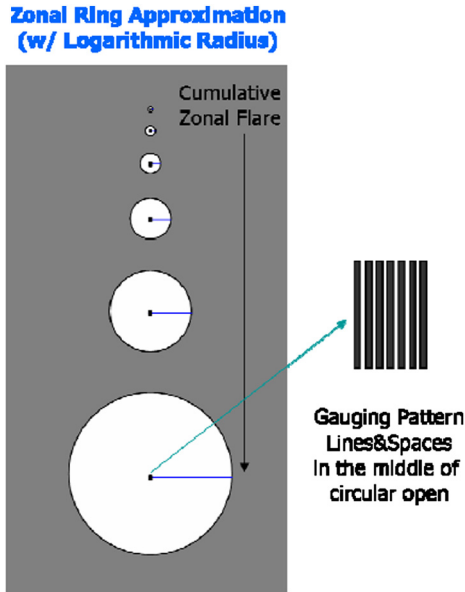


Fig. 8 The zonal ring approximation method (ZRAM) design.<sup>20</sup>

Assume  $I_2$  and  $I_{\text{flare}}$  are the light intensity arriving at the wafer in the reference gauging pattern and the flare intensity from zonal ring, respectively. They have relationships

$$E' = I_2(t_{\text{norm}} + \Delta t) \quad (17)$$

$$E' = (I_2 + I_{\text{flare}})t_{\text{norm}} \quad (18)$$

Combining Eqs. (2) and (15)–(18)

$$\frac{\Delta E}{E_{\text{norm}}} = \frac{I_{\text{flare}}}{I_2} = \frac{I_{\text{ML}} \int_{r_0}^{r_1} \text{PSF}(r) 2\pi r dr}{I_2}, \quad (19)$$

where  $r_0$  and  $r_1$  are the inner and outer radii of the zonal ring, respectively.  $I_{\text{ML}}$  is the light intensity from a large bright field.  $E_{\text{norm}}$  is the normal dose and  $\Delta E$  can be found from the reference CD-to-dose table. Since the gauging pattern is very small, e.g., 50-nm half pitch line/space grating, diffraction should be included in  $I_2$ . Therefore,  $I_2$  can only be calculated from an optical model using simulation software. The absorber EUV and OoB reflection should also be included in the simulation of  $I_2$  if they are comparable to the flare level. The CD is usually measured at the edges of a trench or line feature, and thus,  $I_2$  should be also simulated at the edge of the pattern, too. The pattern edges move with exposure dose, which make the metrology and the  $I_2$  definition more difficult. More work needs to be done for an accurate flare PSF measurement using this method.

The ZRAM has the same advantages as the double-exposure method, e.g., CD measurement instead of visual inspection and use of a small dose instead of a large dose. The resist dependence is removed from ZRAM method, which is an improvement over the double-exposure method. The dose corresponding to the line-width CD difference is extracted using an experimental method, not calculated from a resist model. Of course, the double-exposure method can also remove the resist dependence using the reference CD-to-dose idea. CDU and LER can affect the measurement result. The short-range flare measurement may also be problematic.

Since the gauging pattern is at the center of the zonal ring, addressing and auto-focusing patterns need to be located in the center of the zonal ring, too, as a requirement of the metrology. Thus, the center area inside the inner radius of the zonal ring should not be too small. More work needs to be done on the metrology plan and the  $I_2$  definition issue, as mentioned in the above paragraph, before an accurate PSF measurement can be made using the ZRAM technique.

#### 4 NXE:3100 Flare Measurement Result

The NXE:3100 located at IMEC is the latest preproduction EUV machine from ASML. The flare of this tool has been measured with the Kirk method, and the PSF has been extracted from the measurement result.

Conventional illumination with  $\sigma = 0.81$  and numerical aperture = 0.25 is used in the experiment. Best focus is determined to be  $-0.02 \mu\text{m}$ . The resist used in the experiment is an SEVR-140 of 50-nm thickness.  $E_B$  is measured from a large bright field and determined to be  $4.5 \text{ mJ}/\text{cm}^2$ . A Hitachi CG-4000 CD SEM was used as a metrology tool.

There were three sections on the mask. Kirk donut patterns were located in sections A and B. Section A included 22 donut patterns with a shared 12-mm outer radius. The inner radius ranged from 0.135 to  $80 \mu\text{m}$  in logarithmic steps. Section B included 5 donut patterns with a fixed 2.5-mm outer radius. The inner radius ranged from 100 to  $1000 \mu\text{m}$  logarithmically. Section C is a blank  $3 \times 3 \text{ mm}^2$  area completely covered by an absorber. The EUV and OoB reflection from the absorber can be measured from this section directly. The pattern in Section C and each donut pattern are exposed separately with the aid of reticle masking (REMA) blades. Therefore, flare result from one pattern is not affected by the others.

The OoB reflected from the absorber, the ML, and an aluminum-coated reticle is estimated to be 1.7%, 2.6%, and 4.2%, respectively, after considering the experimental results from section C, the simulated result of EUV absorber reflection, and the ratio result from Table 1 in Ref. 27.

Figure 9 shows the experimental results and the curve fitting of the KF for the NXE:3100. The experimental result of the donut patterns from sections A and B is plotted as circle and star, respectively. The curve fitting of the donut patterns from sections A and B is plotted as solid and dashed lines, respectively. A double-fractal PSF model was used in the curve fitting. The experimental result and the curve-fitted value for KF are 9% and 8.5%, respectively, for a  $2\text{-}\mu\text{m}$  diameter absorber pad placed in a 12-mm outer radius bright field.

Figure 10 shows the simulated double-fractal PSF curve corresponding to the best curve fitting result in Fig. 9. Two single-fractal curves consisting of the solid-line double fractal curve are also plotted as dashed and dotted lines in Fig. 10 for reference. The values for the  $K_1$ ,  $K_2$ ,  $n_1$ , and  $n_2$  parameters are 0.000395, 0.0018, 2.73, and 1.053, respectively. The TIS factor was calculated to be 15.4%.

The fact that the KF in the NXE:3100 is smaller than the 14% KF in the ADT,<sup>8</sup> shows the improvements that have been made in the EUV mirror fabrication. However, the KF in the NXE:3100 was discovered to have increased from 5% in 2011<sup>30</sup> to 8.5% in 2013. This increase could be the result of contamination or material degradation with use and needs to be further addressed.

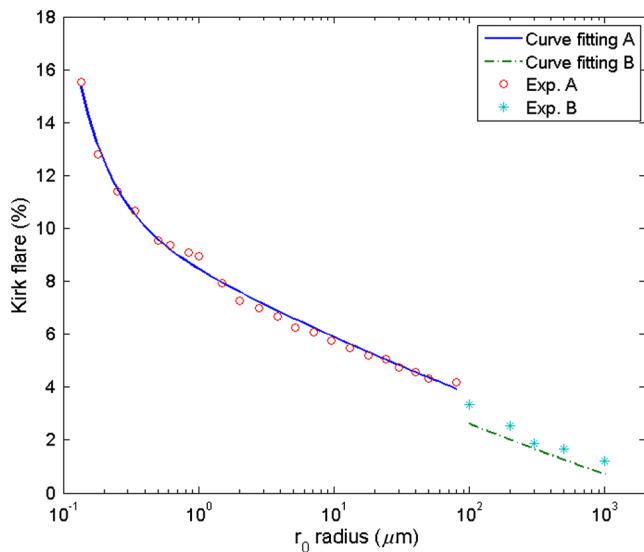


Fig. 9 Experimental and curve-fitted Kirk flare (KF) results from an NXE:3100.

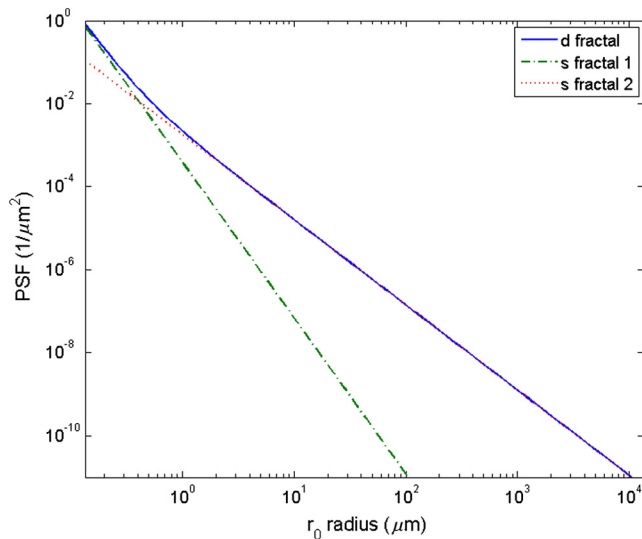


Fig. 10 Double-fractal and the single-fractal PSF curves.

## 5 Conclusion

Four flare measurement methods including Kirk, MTF, double exposure, and ZRAM methods are reviewed and analyzed theoretically in this article. The detailed relationship between measured flare and PSF is analyzed. The PSF of an EUV NXE:3100 exposure tool is extracted from the measured KF and fitted with a double-fractal model. The observation of the increased flare level in the NXE:3100 tool suggests that contamination of EUV optics may be a potential problem for EUVL manufacturing.

## Acknowledgments

The authors thank Chuan Biao Bar from GLOBALFOUNDRIES for reticle tape out, and Markus Bender, Thorsten Schedel, and Martin Bloecker from the Advanced Mask Technology Center in Dresden for reticle fabrication.

## References

1. H. Levinson, *Principles of Lithography*, 3rd ed., SPIE Press, Bellingham, Washington (2011).
2. V. Bakshi, *EUV Lithography*, SPIE Press, Bellingham, Washington (2008).
3. B. Wu and A. Kumar, "Extreme ultraviolet lithography: a review," *J. Vac. Sci. Technol. B* **25**, 1743–1761 (2007).
4. O. Wood et al., "Insertion strategy for EUV lithography," *Proc. SPIE* **8322**, 832203 (2012).
5. Y. C. Kim, P. D. Bisschop, and G. Vandenberghe, "Evaluation of stray light and quantitative analysis of its impact on lithography," *J. Microlith., Microfab., Microsyst.* **4**(4), 043002 (2005).
6. M. D. Smith et al., "Comprehensive EUV lithography model," *Proc. SPIE* **7969**, 796906 (2011).
7. Y. C. Kim, P. D. Bisschop, and G. Vandenberghe, "Characterization of stray light of ArF lithographic tools: modeling of power spectral density of an optical pupil," *Microelectron. Eng.* **83**, 643–646 (2006).
8. J. Moon et al., "Comparison of simulation and wafer results for shadowing and flare effect on EUV Alpha Demo Tools," *Proc. SPIE* **7520**, 75200T (2009).
9. M. Arnz, "Flare metrology used for PSD reconstruction," *Proc. SPIE* **5835**, 178–187 (2005).
10. M. Shirraishi et al., "Flare modeling and calculation for EUV optics," *Proc. SPIE* **7636**, 763629 (2010).
11. J. P. Kirk, "Scattered light in photolithographic lenses," *Proc. SPIE* **2197**, 566–572 (1994).
12. C. A. Mack, "Measuring and modeling flare in optical lithography," *Proc. SPIE* **5040**, 151–161 (2003).
13. H. Aoyama et al., "Flare evaluation for 32-nm half pitch using SFET," *Proc. SPIE* **6921**, 69213H (2008).
14. A. Grassmann and H. Moritz, "Contrast transfer function measurements of deep ultraviolet steppers," *J. Vac. Sci. Technol.* **B10**(6), 3008–3011 (1992).
15. B. LaFontaine et al., "Analysis of flare and its impact on low-k1 KrF and ArF lithography," *Proc. SPIE* **4691**, 44–56 (2002).
16. S. H. Lee, D. A. Tichenor, and W. P. Ballard, "Lithographic evaluation of the EUV engineering test stand," *Proc. SPIE* **4688**, 266–276 (2002).
17. B. LaFontaine et al., "Characterization, modeling and impact of scattered light in low-k1 lithography," *Proc. SPIE* **5754**, 285–293 (2005).
18. A. Bourov, L. C. Litt, and L. Zavvalova, "Impact of flare on CD variation for 248-nm and 193-nm lithography systems," *Proc. SPIE* **4346**, 1388–1393 (2001).
19. L. C. Litt et al., "Evaluation and characterization of flare in ArF lithography," *Proc. SPIE* **4691**, 1442–1452 (2002).
20. I. Kim et al., "Methodology of flare modeling and compensation in EUVL," *Proc. SPIE* **7140**, 714009 (2008).
21. T. Uno et al., "Challenges in flare correction in EUVL lithography for half pitch 22-nm generation," *Proc. SPIE* **7748**, 774826 (2010).
22. R. Inanami et al., "Study of practical TAT reduction approaches for EUV flare correction," *Proc. SPIE* **7636**, 763616 (2010).
23. K. Murakami, T. Oshino, and H. Kondo, "Development progress of optics for extreme ultraviolet lithography at Nikon," *J. Micro/Nanolith. MEMS MOEMS* **8**(4), 041507 (2009).
24. H. S. Seo et al., "Absorber stack optimization in EUVL masks: lithographic performances in alpha demo tool and other issues," *Proc. SPIE* **7636**, 76360X (2010).
25. S. A. George et al., "Assessing out-of-band flare effects at the wafer level for EUV lithography," *Proc. SPIE* **7636**, 763626 (2010).
26. G. F. Lorusso et al., "Flare in extreme ultraviolet lithography: metrology, out-of-band radiation, fractal point-spread function, and flare map calibration," *J. Micro/Nanolith. MEMS MOEMS* **8**(4), 041505 (2009).
27. G. F. Lorusso et al., "Metrology development for extreme ultraviolet lithography: flare and out-of-band qualification," *J. Vac. Sci. Technol. B* **29**, 06F505 (2011).
28. L. Sun et al., "Fourier spectrum method to determine dose-to-clear in a photoresist," *Opt. Lett.*, accepted (2013).
29. M. Chandhok et al., "Comparison of techniques to measure the point spread function due to scatter and flare in EUV lithography systems," *Proc. SPIE* **5374**, 854–860 (2004).
30. C. Wagner et al., "EUV lithography at chipmakers has started: performance validation of ASML's NXE:3100," *Proc. SPIE* **7969**, 79691F (2011).

Lei Sun is the principal engineer in the lithography R&D group at GLOBALFOUNDRIES with a focus on 7-nm node semiconductor technology. His research field includes flare, EUV mask 3-D effect, overlay, phase shift mask, and device integration. He received his BS, MS from Nankai University in 2001 and 2004, and PhD degree from University of Rochester with a major in optics in 2009. He also has 9 years experience in laser and fiber optics. He is author or co-author of 36 technical papers and inventor or co-inventor of 9 patents. He is a member of SPIE and Optical Society of America.

**Obert Wood** is a principal member of technical staff in the Strategic Lithography Technology Department at GLOBALFOUNDRIES. He was a member of technical staff at Bell Laboratories for 34 years and has extensive experience in extreme-ultraviolet lithography, ultra-high intensity lasers, and laser surgery. He received his BS, MS, and PhD degrees from the University of California at Berkeley in electrical engineering in 1964, 1965, and 1969. He is author or co-author of 258 technical papers and inventor or co-inventor of 24 patents and is a fellow of the Optical Society of America, a senior member of IEEE, and a member of the AAAS, the American Physical Society, the American Vacuum Society, and SPIE.

**Erik Verduijn** is member of technical staff in the strategic lithography R&D group at GLOBALFOUNDRIES and assigned to the IMEC research consortium. At IMEC, he supports GLOBALFOUNDRIES' EUVL research activities related to mask defectivity, resist optimization, device integration, and printability enhancements. He received his licence de physique in fundamental physics from the Université de Rouen in 1999 and MSc in applied physics from Eindhoven University of Technology in 2002, followed by 5 years of PhD research on spin polarization and tunneling magnetoresistance of Heusler half metals at the Ruhr-Universität Bochum. He has 7 years experience in the semiconductor industry in the fields of lithography and atomic layer deposition and having worked previously at ASML and ASM.

**Mandeep Singh** is senior member in GLOBALFOUNDRIES' technical staff in Strategic Lithography Technology and assigned to the IMEC research consortium, where his research activities are related to lithography.

**Wenhui Wang** is litho engineer at GLOBALFOUNDRIES. His research field includes multiple patterning for advanced technology nodes, mask 3-D effects, overlay, and on-product focus monitoring. He received his BS, MS from Zhejiang University in 1998 and 2001, and PhD degree from Shanghai Institute of Microsystem and Information Technology with a major in solid physics and microelectronics in 2004. He also has years of experience in MEMS and fiber optics.

**Ryong-han Kim** received his PhD from electrical engineering at Texas A&M University, College Station, Texas, with a topic of integrated optics. Currently, he is working in lithography R&D group at GLOBALFOUNDRIES with a focus on sub-10 nm node technology develop. His research focus is technology definition which encapsulates lithographic process and modeling, integration, and design-technology co-optimization (DTCO).

**Pawitter Mangat** is presently the deputy director of EUV lithography at GLOBALFOUNDRIES and responsible for establishing EUVL infrastructure while mitigating key technical challenges and providing manufacturable solutions for foundry business. Previously, he held leadership roles at Motorola Inc. managing global/virtual teams in multidisciplinary projects and was SRC Board of Directors and SIA Technology Strategy Committee member. He holds a PhD degree in materials science (1991) and MBA degree in technology management (2000). He has 24 issued patents and co-authored 100+ publications.

**Hui Peng Koh** received her master's degree in materials engineering from Nanyang Technology University of Singapore. She joined Chartered Semiconductor Singapore in 2000 and worked on process development for advanced technology nodes in Technology Development Division. For the past 2.5 years, she has relocated to New York to lead the EUV lithography program to coordinate the installation of EUV lithography equipment and processes in GLOBALFOUNDRIES development fab.

**Harry Levinson** is a senior fellow and manager of GLOBALFOUNDRIES's Strategic Lithography Technology Department, which is responsible for advanced lithographic processes and equipment. He has published numerous articles on lithographic science and is the author of two books: *Lithography Process Control* and *Principles of Lithography*. He is an SPIE fellow. He has a BS degree in engineering from Cornell University and a PhD degree in physics from the University of Pennsylvania.